JMEPEG
https://doi.org/10.1007/s11665-024-10512-8

1059-9495/$19.00

ORIGINAL RESEARCH ARTICLE

The Effect of Energy Density on Microstructural, Mechanical, and Corrosion Characteristics of Ti-6Al-4V Alloy Fabricated via Selective Laser Melting and Electron Beam Melting Techniques

H. Yilmazer, Y.A. Sadikoglu, S. Kucuk, O. Gokcekaya, I.C. Turu, T. Nakano, and B. Dikici

Submitted: 25 March 2024 / Revised: 23 August 2024 / Accepted: 14 September 2024

In this study, the effect of production parameters on Ti-6Al-4V alloys fabricated using selective laser melting (SLM) and electron beam melting (EBM) techniques was investigated. Through the variation of energy volume (12.5, 25, 37.5 J mm^{-3}), these two additive manufacturing methods were compared in terms of microstructure, mechanical, and corrosion properties. Density was calculated using Archimedes' technique, while microstructure was characterized through optical microscopy (OM) and scanning electron microscopy (SEM). Mechanical properties were determined via micro-Vickers hardness and tensile tests. Electron backscatter diffraction (EBSD) and x-ray diffraction (XRD) analyses were performed on EBM and SLM samples for a comprehensive understanding. Corrosion susceptibilities of the alloys were evaluated using potentiodynamic scanning (PDS) tests in a 3.5% NaCl solution at room temperature. Microstructural analysis revealed that SLM-produced parts predominantly consisted of the α' (martensite) phase, whereas EBM-produced parts primarily comprised the α phase with a small amount of the β phase. The strength values of all SLM samples exceeded 930 MPa, surpassing those of wrought Ti-6Al-4V ELI. However, only EBM samples fabricated with a 37.3 J mm^{-3} energy volume approached this standard. Corrosion susceptibility generally increased with higher energy volume in both EBM and SLM samples, with porosity volume and grain size variations influencing corrosion behavior.

Keywords Corrosion, EBM, Energy density, Phase transformation, SLM, Ti-6Al-4V

1. Introduction

Additive manufacturing (AM), also known as 3D printing, is an advanced manufacturing process that has been rapidly growing in popularity due to its ability to produce complex geometries and parts with superior mechanical properties. Among the various AM techniques, selective laser melting (SLM) and electron beam melting (EBM) stand out as two of the most widely adopted methods for producing metallic parts (Ref 1, 2). While both SLM and EBM involve the layer-by-layer fusion of powder particles to create three-dimensional objects, they differ significantly in their energy sources and operating environments (Ref 3). SLM utilizes a high-powered laser to melt metal powders in an inert gas atmosphere, whereas EBM employs an electron beam in a vacuum chamber. These distinct processing conditions lead to differences in the microstructure and properties of the parts produced (Ref 4). These differences make SLM more suitable for applications requiring high precision and surface finish, while EBM is favored for producing components that require high strength and durability with lower residual stresses (Ref 5). Both techniques have shown great promise in the production of high-performance aerospace, automotive, and medical parts due to their high precision and accuracy (Ref 4, 6).

Titanium alloys are commonly used in various industries due to their excellent mechanical properties, including high strength-to-weight ratio, improved corrosion resistance, and good biocompatibility. The Ti-6Al-4V alloy is a widely used titanium alloy due to its high strength, low density, and excellent corrosion resistance (Ref 7). However, the traditional manufacturing processes for Ti-6Al-4V alloy parts, such as casting and forging, have several limitations in terms of producing complex geometries and achieving desirable microstructures (Ref 8).

In recent years, SLM and EBM have emerged as promising AM techniques for the production of Ti-6Al-4V alloy parts (Ref 9). These techniques allow for the production of complex

H. Yilmazer, Department of Metallurgical and Materials Engineering, Yildiz Technical University, 34220 Istanbul, Turkey; and Health Biotechnology Joint Research and Application Center of Excellence, 34220 Istanbul, Turkey; **Y.A. Sadikoglu** and **S. Kucuk**, Department of Metallurgical and Materials Engineering, Yildiz Technical University, 34220 Istanbul, Turkey; and **O. Gokcekaya** and **T. Nakano**, Division of Materials and Manufacturing Science, Osaka University, Osaka 565-0871, Japan; and Anisotropic Design and Additive Manufacturing Research Center, Osaka University, Osaka 565-0871, Japan; **I.C. Turu**, Department of Metallurgical and Materials Engineering, Yildiz Technical University, 34220 Istanbul, Turkey; and Department of Mechanical Engineering, Adiyaman University, 02040 Adiyaman, Turkey; and **B. Dikici**, Department of Mechanical Engineering, Ataturk University, 25240 Erzurum, Turkey. Contact e-mail: burakdikici@atauni.edu.tr.

Published online: 10 December 2024

geometries and the ability to achieve desirable microstructures through the manipulation of various processing parameters. However, the effects of the processing parameters on the microstructure, mechanical properties, and corrosion resistance of Ti-6Al-4V alloy parts produced by SLM and EBM have not been fully investigated (Ref 10).

The microstructure of Ti-6Al-4V alloy, produced using SLM and EBM techniques with varying energy density, has been extensively examined in prior research (Ref 11, 12). In a study conducted by Ren et al. (Ref 13) in 2020, a comparison was made between the microstructures and mechanical properties of Ti-6Al-4V fabricated through SLM and EBM. This research delved into the impact of process parameters on the microstructure and resulting mechanical properties of Ti-6Al-4V alloy. The findings revealed that SLM Ti-6Al-4V alloys exhibited martensitic structures, enhancing their hardness in comparison with EBM Ti-6Al-4V alloys. Additionally, Toh et al. (Ref 14) explored the microstructure and wear properties of EBM-manufactured Ti-6Al-4V components in comparison with conventionally cast Ti-6Al-4V samples in a 2016 study. The results demonstrated that EBM-produced Ti-6Al-4V parts exhibited a finer microstructure and higher hardness compared to conventionally cast Ti-6Al-4V samples.

Hardness comparisons of SLM and EBM Ti-6Al-4V alloys have also been extensively studied (Ref 15-17). Rafi et al. (Ref 17) conducted a comprehensive benchmark comparison on microstructure, mechanical properties, and their underlying mechanisms in SLM and EBM Ti-6Al-4V alloys. The study found that the existence of martensite microstructure in the SLM-printed Ti-6Al-4V sample enhanced the hardness property compared to EBM Ti-6Al-4V samples. Additionally, a study by Zhang et al. (Ref 15) examined the wear properties of Ti-6Al-4V alloy as prepared by SLM, EBM, and conventional casting methods. The results showed that the SLM and EBM Ti-6Al-4V samples had higher hardness and wear resistance than conventionally cast samples.

The corrosion properties of SLM and EBM Ti-6Al-4V alloys with varying energy density were investigated. Several studies have highlighted differences in corrosion resistance between these AM techniques. Yu et al. (Ref 18) compared the corrosion behavior of Ti-6Al-4V alloy fabricated using SLM, EBM, and ISF, demonstrating that SLM-produced samples exhibited superior corrosion resistance, primarily due to their denser microstructure and absence of preheating-induced stresses. Another study by Zhou et al. (Ref 19) investigated the microstructural influence on the corrosion behavior of SLM-manufactured Ti-6Al-4V and found that SLM samples had a higher corrosion resistance than conventionally cast samples. These studies underscore the significant impact of microstructural variations on the corrosion performance of Ti-6Al-4V alloys, which is critical for their application in industries where corrosion resistance is paramount, such as aerospace and biomedical fields. Fojt et al. (Ref 20) studied the corrosion properties and biocompatibility of Ti-6Al-4V alloy manufactured using SLM and EBM. The results showed that the corrosion resistance of SLM-produced samples is generally higher than that of EBM samples, with localized corrosion observed more frequently on the original as-printed surfaces, especially in environments containing fluoride ions. Surface treatment by grinding minimized the risk of local attack. In another study, the microstructure and corrosion behavior of Ti-6Al-4V alloys fabricated using laser powder bed fusion (LPBF) and EBM were investigated by Zadeh et al. (Ref 21). The study revealed that the LPBF-manufactured alloy exhibited significantly better corrosion resistance than the EBM-manufactured alloy. This is primarily due to the formation of a uniform α' martensitic microstructure in LPBF, which reduces the formation of local galvanic cells, a key factor in corrosion resistance. In contrast, EBM-processed alloys tend to develop a dual-phase α/β microstructure, which is more susceptible to corrosion due to the presence of galvanic cells and associated microstructural defects.

As seen in the literature, there are various factors that can affect the properties of parts produced using SLM or EBM techniques. Previous studies have examined the influence of production parameters on the microstructure and mechanical properties of SLM and EBM parts, including laser power, scanning speed, and layer thickness. However, the relationship between production parameters and energy density has not been fully investigated. Thus, in this study, the effect of production parameters on the density, microstructure, mechanical properties, and corrosion resistance of Ti-6Al-4V alloy produced by SLM and EBM techniques was investigated. In other words, a relationship was established between production parameters and the concept of energy density to compare the two different printing techniques.

2. Experimental Methods

2.1 Sample Preparations

The SLM and EBM samples were produced using commercially available EOS Ti-6Al-4V alloy powders with a particle size distribution of 41 $\pm$ 3 μm (d50) and 76 $\pm$ 6 μm (d90), respectively, manufactured by gas atomization. The Ti-6Al-4V samples were fabricated by implementing a bidirectional scan strategy (X-scan) with dimensions of 10 $\times$ 10 $\times$ 20 mm using two different AM techniques, selective laser melting (SLM) and electron beam melting (EBM). The energy density used in the fabrication process was changed to three different levels of 12.5, 25, and 37.5 J mm^{-3}. The other parameters used in the production process for EBM and SLM technique are presented in Tables 1 and 2 with sample IDs, respectively. However, due to the expected 60% efficiency of the laser process, SLM samples was designed in this energy range to be comparable with the EBM process. Thus, 60% of 20.8, 41.7, and 62.5 J mm^{-3} is equal to 12.5, 25, and

Table 1 Production parameters of Ti-6Al-4V EBM samples

	Sample IDs		
Parameter	**EBM-1**	**EBM-2**	**EBM-3**
Voltage, V	60	60	60
Current, mA	5	10	15
Speed, mm s^{-1}	4000	4000	4000
Line offset, mm	0.1	0.1	0.1
Thickness, mm	0.06	0.06	0.06
Focus offset, mA	10	10	10
Linear energy, J mm^{-1}	75	150	225
Energy volume, J mm^{-3}	12.5	25	37.5

Table 2 Production parameters of Ti-6Al-4V SLM samples

Parameter	Sample IDs		
	SLM-1	SLM-2	SLM-3
Laser power, mW	150	300	360
Speed, mm s^{-1}	1200	1200	960
Hatch, mm	0.100	0.100	0.100
Thickness, mm	0.06	0.06	0.06
Linear energy, J mm^{-1}	12.5	25	37.5
Energy volume, J mm^{-3}	20.8	41.7	62.5
Efficient E volume %60 of V_E, J mm^{-3})	12.5	25	37.5

37.5 J mm^{-3}, respectively. The table temperature for the EBM process was set at 540 °C.

2.2 Microstructural Characterization

The SLM and EBM materials were cut into 10 × 10 × 10 mm using wire electrical discharge machining (WEDM). The samples were abrasively ground (up to 4000 grit) and then polished using a 50 nm silica suspension. All samples were etched in Kroll's reagent (2 vol.% HF, 6 vol.% HNO_3, and 92 vol.% H_2O) for metallographic analyses. Initial observations were conducted using an optical microscope (OM, Olympus NIS-Elements Version 4.3). X-ray diffraction (XRD, Bruker Discovery D8) measurements were carried out with a CuKα radiation (wavelength of 1.54 Å) for phase analysis of the alloys. The XRD analysis was performed with an acceleration voltage of 35 kV and 40 A current, scanning at a step of 0.02 ° per second in the range of 20-80°. Electron back scatter diffraction (EBSD) measurements were conducted using a field-emission scanning electron microscope (FE-SEM, JEOL JIB-4610F) equipped with an EBSD detector (Aztec HKL, Oxford Instruments). The EBSD analysis was performed at an accelerating voltage of 20 kV with a step interval of 2 μm. The obtained data were analyzed using HKL Channel5 analysis software (Oxford Instruments) to generate Inverse Pole Figure (IPF) maps and the corresponding pole figures. All analyses were conducted on surfaces parallel to the build direction.

2.3 Mechanical Tests

Hardness tests were performed using the Vickers test method with a 1 kgf load and a dwell time of 20 s under room temperature conditions. Each sample was tested at eight different random locations to obtain accurate and representative results. All data represent means ± standard deviation of measured values. The tensile tests were conducted at room temperature using a universal tensile test machine (Instron 5982). The tensile speed was set at 0.01 mm/s. For the tensile tests, specimens with a length of 14 mm were prepared using WEDM. A special aperture was fabricated to securely hold the specimens during testing.

2.4 Electrochemical Corrosion Tests

The corrosion tests were carried out in 3.5% NaCl solution at room temperature using potentiodynamic polarization (PDS) by a potentiostat/galvanostat (Gamry). In all electrochemical experiments, the three-electrode technique was used, using a saturated calomel electrode as reference electrode (RE), a pair of graphite rods as a counter electrode (CE), and SLM and EBM samples prepared as working electrode (WE). Before the PDS and EIS tests, open-circuit potential (OCP) values were recorded until a stable equilibrium state. For PDS tests, the samples were polarized in the cathodic and anodic directions at scanning speeds of 1 mV/s, starting from −300 mV below the OCP value and up to the 2.5 V andic potential values. The acquired data were standardized to the field and analyzed using the device's Echem Analyst software.

3. Results and Discussion

In Fig. 1, optical microscope images of the samples produced using SLM and EBM techniques with varying energy volumes are presented after the polishing process.

In both EBM and SLM samples, there was a proportional decrease in pore quantity with the increase in energy volume (Fig. 1). Additionally, in SLM samples, there was a proportional reduction in pore size as the laser power increased (Fig. 1d-f). Specifically, samples produced with lower energy volume values in both EBM and SLM (Fig. 1a and d) exhibited numerous irregular pores marked by red arrows in Fig. 1. These irregular pores were primarily the result of insufficient melting, also known as lack of fusion (LOF). Furthermore, some spherical gas pores were also observed in the samples, indicated by red circles in Fig. 1. In the EBM samples, the gas porosity was found to be less than 20 μm, whereas in the SLM samples, the gas porosity was observed to be less than 10 μm. These pores were attributed to inadequate process parameters and trapped argon gas, a byproduct of powder production. As energy input increased, the occurrence of these LOF defects decreased, and spherical gas pores became more prevalent, especially in higher energy samples. Remarkably, irregular pores resulting from incomplete melting were absent in the EBM-3 and SLM-3 samples (Ref 22). It can be concluded that while inappropriate process parameters primarily caused irregular pores, often referred to as LOF, spherical pores were formed due to trapped argon gas between titanium powders during powder production (Ref 11, 23). Consequently, increasing the energy volume in the EBM samples eliminated defects caused by partial melting, leading to the formation of a denser structure. In the SLM samples, with the decrease in scanning speed and increase in laser power, the problem of insufficient melting disappeared, and irregularly shaped pores were not observed in the SLM-3 sample. Therefore, the increase in the energy volume caused a decrease in the occurrence of LOF-related pores in the SLM samples as well as in the EBM samples, leading to a shift toward spherical gas pores in higher energy inputs. According to Montalbano et al. (Ref 24) in the PBF technique when the energy density increases, small spherical gas pores appear instead of irregularly shaped pores which were caused by the lack of fusion. Moreover, although there were some microstructural differences between EBM and SLM samples, the results of porosity analysis indicated that the porosity levels of the SLM samples were comparable to those of the EBM samples.

The images obtained from the polished surfaces of the samples (not limited to the above) were utilized to calculate the maximum pore size and assess the relative densities of the samples (Fig. 2).

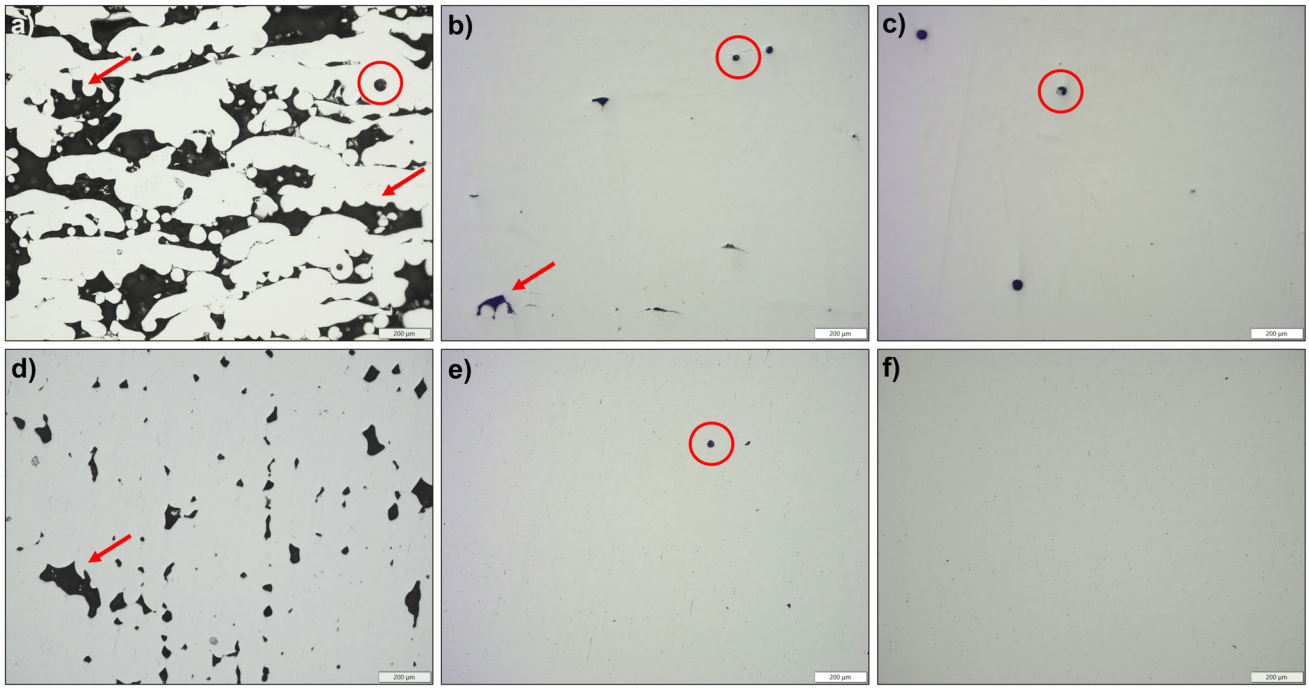

Fig. 1 The optical microscope images of samples after post-polishing: (a) EBM-1, (b) EBM-2, (c) EBM-3, (d) SLM-1, (e) SLM-2, and (f) SLM-3

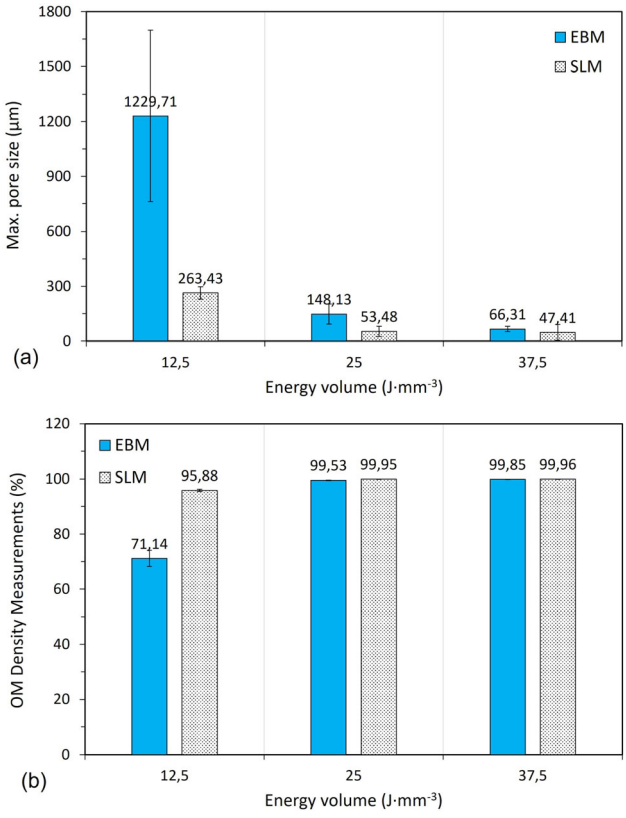

Fig. 2 Maximum pore size and density measurements from polished sample surfaces

Figure 2 illustrates that the relative density of the samples increased while the maximum pore size decreased with the rise in energy volume values. Furthermore, the relative densities of the components produced through both EBM and SLM techniques were determined using the Archimedes method (Fig. 3).

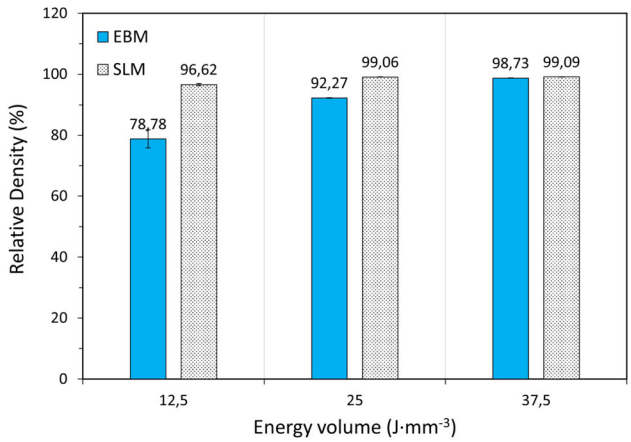

Fig. 3 Relative densities of EBM and SLM samples determined using the Archimedes method

It was observed that the densities of EBM-manufactured Ti-6Al-4V parts significantly increased as the energy density rose. In contrast, the density of SLM parts did not show a notable increase with the growing energy volume, as even high bulk densities could be achieved at low-energy volume values in SLM. When the energy volume of the EBM-produced parts reached 37.5 J mm^{-3}, their relative densities matched those of SLM-produced parts. Liu and Shin (Ref 9) reported that the quantity of pores, a characteristic feature of AM, can be reduced through the optimization of process parameters. However, completely eliminating these pores does not allow for achieving the theoretical density attained through traditional manufacturing methods.

Figure 4 presents that OM images following the etching process of EBM and SLM samples, produced with an energy volume of 37.5 J mm^{-3}, are presented.

The microstructures of EBM Ti-6Al-4V alloys reveal an $\alpha + \beta$ microstructure characterized by a thin lamellar structure and prior β grain boundaries (α grain boundaries) undergoing diffusional transformation (Ref 16). Specifically, the β phase undergoes diffusional transformation at the grain boundaries, converting into the α phase due to the slow cooling inherent in the EBM technique, which requires a high base temperature (~540 °C). In Fig. 4a-c, Widmanstätten α plates and β grain boundaries are clearly visible, indicating partial transformation. Briefly, a typical $\alpha + \beta$ microstructure with a basketweave morphology is observed in EBM samples (Fig. 4a, b), while a primary β columnar grain boundary around the α grain boundary is evident (Fig. 4c). Conversely, preheating is not employed in the SLM technique, resulting in rapid cooling, and the primary β phase remains undiffused at the grain boundaries (Fig. 4d). This indicates that the β-phase is either absent or below the detection limit of XRD in our SLM-produced parts. Primary β grains elongate along the build direction, and needle-like martensitic-like α'/α colonies are also present (Fig. 4c). Gong et al. (Ref 16) explored the microstructures of SLM-produced parts, revealing a predominant needle-like α' martensite phase. The primary microstructure of SLM Ti-6Al-4V comprises prior β phase at the grain boundaries and the needle α' martensite phase (Ref 25). Notably, no martensitic structure was identified in the EBM parts due to slow cooling. The microstructure of EBM Ti-6Al-4V includes columnar prior β grains defined by wavy grain boundary α and transformed α/β structures with both colony and basket-wave morphology, along with numerous singular α platelets within the prior β grains (Ref 26, 27).

Microstructural examinations have revealed that Ti-6Al-4V parts produced through SLM primarily consist of the α' (martensite) phase, while those produced through EBM are primarily composed of the α phase with a small amount of β phase (Ref 11, 17, 25, 28, 29). These findings align with numerous studies in the literature (Ref 11, 28). Figure 5 displays the XRD graph of samples produced through AM.

In the as-built state of Ti-6Al-4V alloy produced with EBM and SLM, prominent peaks of α/α' are observed at (100), (002), (101), and (102) planes. Conversely, in parts produced through EBM, a β peak at 71 ° corresponding to the (211) plane is observed, while this phase is not observed in parts produced through SLM, except for SLM-3 (Fig. 6). This suggests that all SLM parts are predominantly composed of the α/α' phase, given the absence of preheating in the SLM technique, leading to faster cooling compared to EBM parts. However, SLM-3, produced with high energy, exhibits a minor β phase with a (110) orientation. Additionally, the XRD pattern of the EBM-1 sample is shifted to the left compared to other patterns, attributed to higher strain.

EBSD analyses were conducted on the samples to examine in detail the crystallographic orientations within the microstructure, as well as grain and phase boundaries. Microstructural analysis was conducted on Ti-6Al-4V samples produced through EBM and SLM with energy volumes of 12.5, 25, and 37.5 J mm^{-3}, respectively, using EBSD. The analyses were performed on the surfaces of the samples parallel to the built direction (yz plane) to observe microstructural changes. In Fig. 7, inverse pole figures (IPFs) of EBM and SLM Ti-6Al-4V samples are presented, revealing variations in the orientation of α grains. Different colors in the IPF maps correspond to crystallographic orientations of α grains, where red, green, and blue represent the $(0001), (\bar{1}2\bar{1}0), (01\bar{1}0)$ planes, respectively.

EBM Ti-6Al-4V samples demonstrated an increase in average grain size corresponding to higher beam energy density, reaching 1.71 μm for EBM-3, attributable to the elevated preheat temperature. In contrast, SLM Ti-6Al-4V exhibited a decrease in grain size with escalating laser energy densities, as depicted in Fig. 8a and c. This findings are

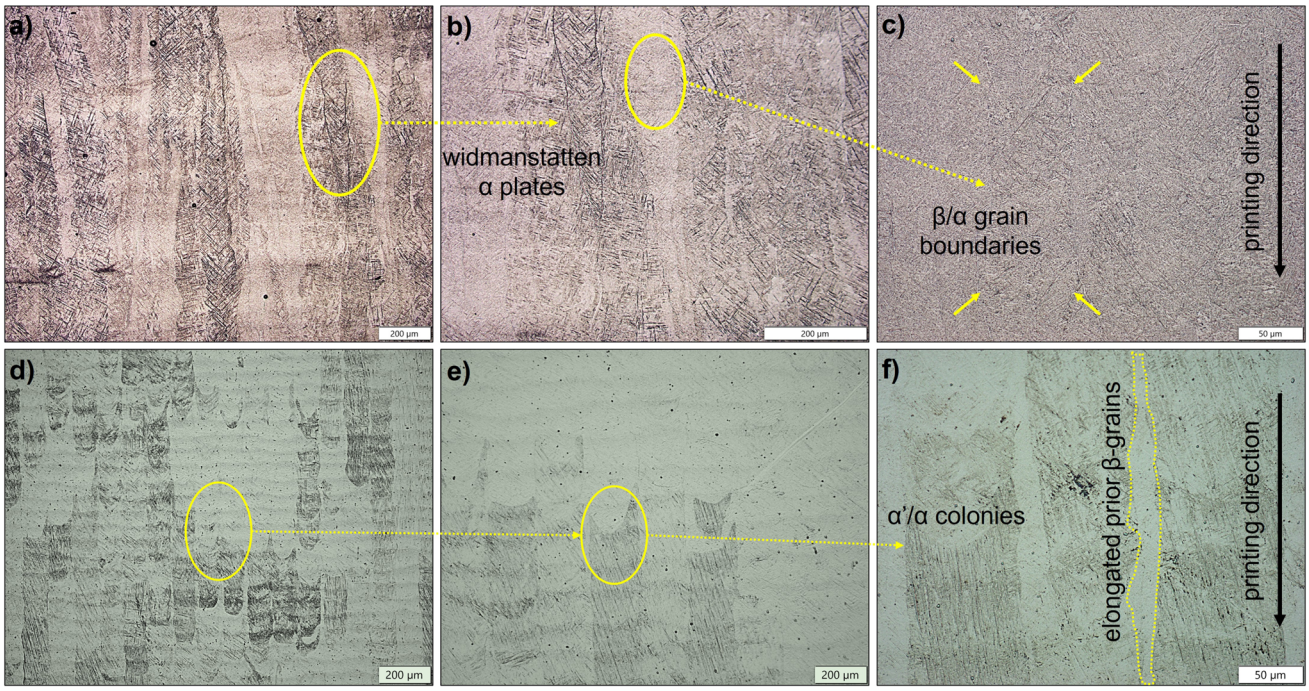

Fig. 4 OM images after etching of EBM and SLM samples produced with an energy volume of 37.5 J mm^{-3} at different magnifications

consistent with those of Han et al. (Ref 30), who reported that higher laser energy density results in a larger prior-β grain width and a smaller α' martensite size for SLM Ti-6Al-4V samples. EBM-1 displayed a higher grain size than EBM-2, with fusion defects exceeding 20% of the optical density, attributed to irregularities in melt pool formation. The irregular grain formation in EBM-1 can be discerned through the grain characteristics as shown in Fig. 8b and d. As the beam energy increased from EBM-2 to EBM-3, the ratio of recrystallized grains increased, while the ratio of deformed grains decreased, a trend not observed in EBM-1. Additionally, SLM Ti-6Al-4V samples exhibited an increase in recrystallized grain rate with rising laser energy density.

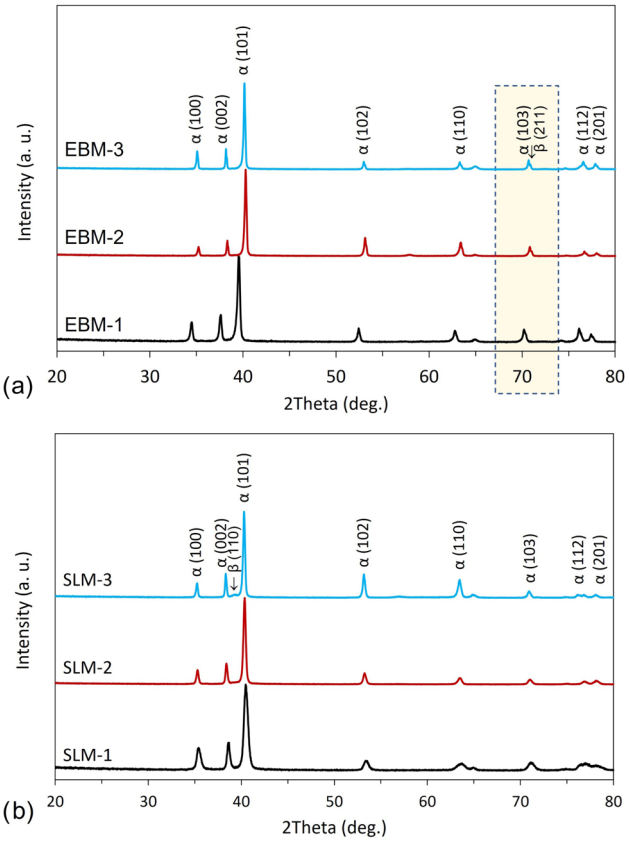

Fig. 5 XRD graph of the as-built microstructures of Ti-6Al-4V alloy produced through (a) EBM and (b) SLM techniques

IPF maps of EBM samples revealed thicker α laths with a 45° tilt from the build direction (BD) due to the high-energy input, facilitating the epitaxial growth of (100) β grains along multiple layers. In contrast, SLM samples exhibited acicular α' martensite laths with random tilts from BD, influenced by the weak texture of the parent β phase. It has been noted that there exists an orientation relationship between α and β phases during the $\alpha \longleftrightarrow \beta$ phase transformation, referred to as Burger's orientation relationship (BOR). Burger's orientation relationship is defined as $(0001)\alpha \parallel (110)\beta$ and $(11\bar{2}0)\alpha \parallel (1\bar{1}1)\beta$ (Ref 31). According to BOR, there are 12 α variants that may form in a β grain during the $\beta \rightarrow \alpha$ phase transformation.

In the context of EBM, the well-established α variant selection was achieved through a high preheat temperature, promoting (100) β grains, and a subsequent slow cooling rate that prevented thermal and phase-transformation stresses, as illustrated in Fig. 9 with corresponding multiples of uniform distribution (MUD). MUD is a measure of the texture strength in an EBSD pole figure, with higher values indicating stronger alignment. EBM-1 exhibited random variant selection with MUD = 4.92 due to irregular melt pool formation, while EBM-3 demonstrated six α variant selections with MUD = 19.66. Furthermore, EBM-2 displayed a distinct variant selection with MUD reaching 31.21, indicating a lower grain boundary misorientation between α grains. However, in the case of SLM without preheating, stresses arise during phase transformation due to the volume difference between the α and β phases, influencing α variant selection and resulting in a random α texture (Ref 32), yielding lower MUD in the range of 11.90 to 12.37 compared to EBM samples.

The hardness test results of Ti-6Al-4V alloys produced with different energy volumes through EBM and SLM are presented comparatively in Fig. 10.

The hardness of both EBM and SLM parts increased with the rise in energy volume. The heightened hardness in SLM samples is attributed to the high dislocation and heterogeneity in the martensitic structure as energy volume increases. In EBM samples, the increase in hardness is primarily linked to a

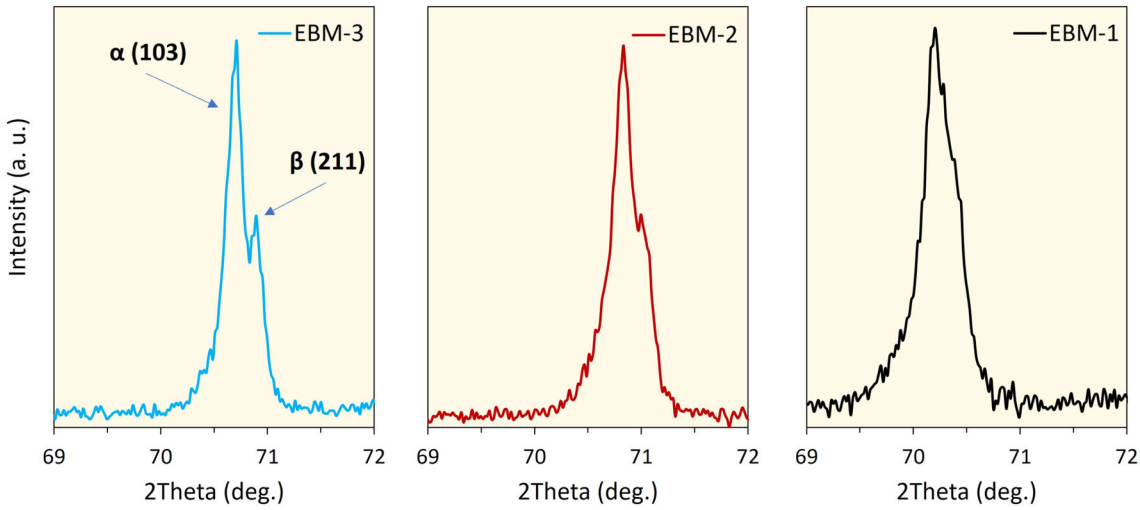

Fig. 6 Magnified view of the region indicated by the rectangular-dashed line and shaded in yellow in the XRD graph presented in Fig. 5

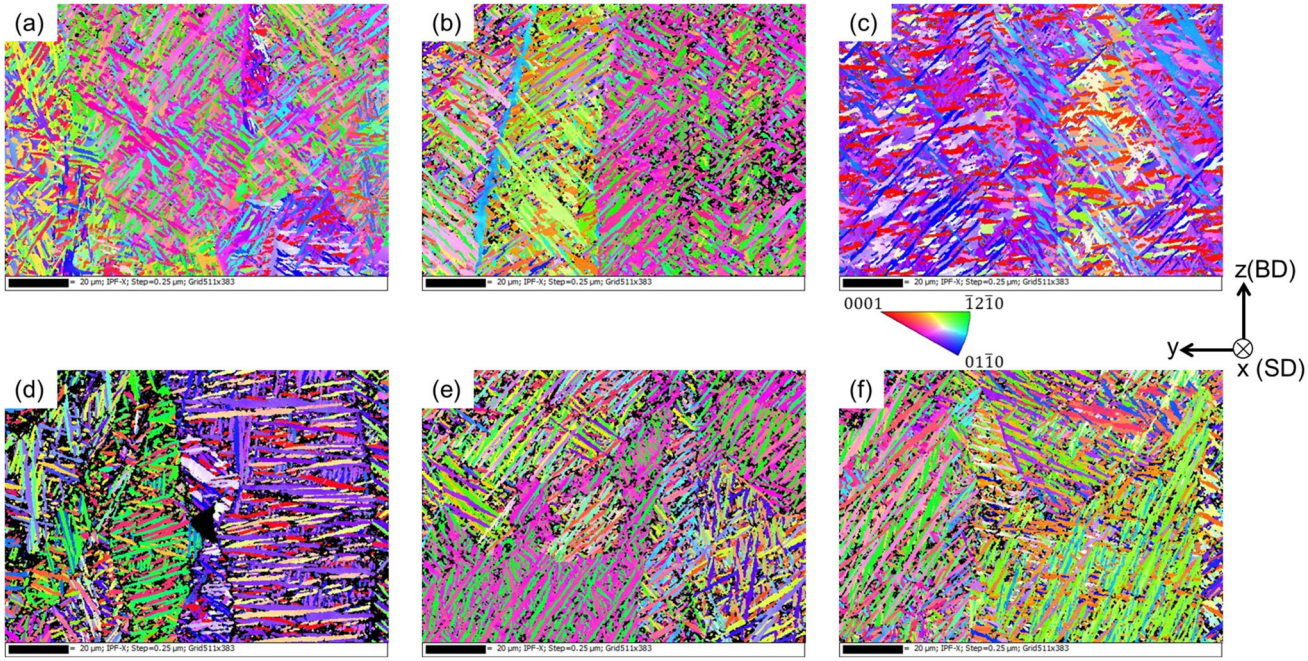

Fig. 7 Inverse pole figures of (a) EBM-1, (b) EBM-2, (c) EBM-3, (d) SLM-1, (e) SLM-2, and (f) SLM-3

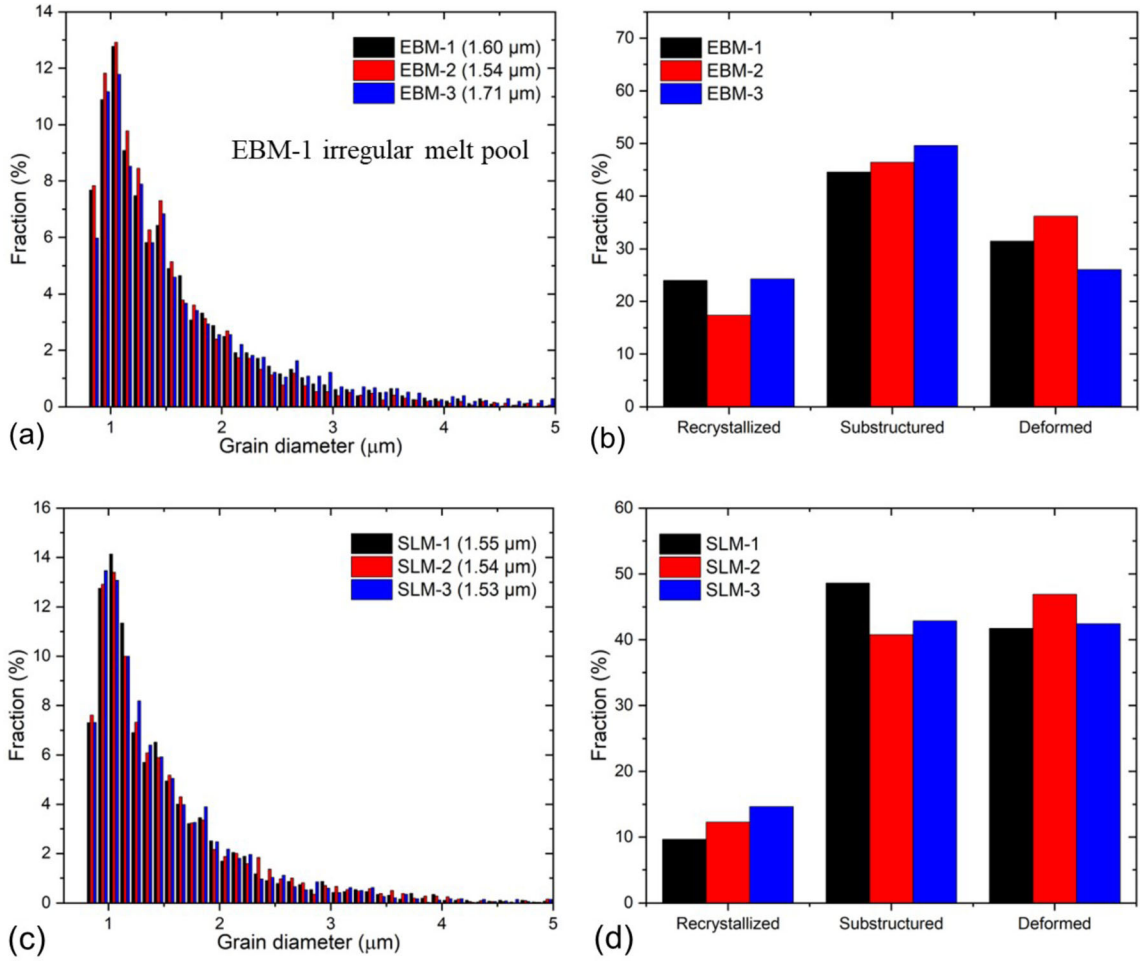

Fig. 8 Grain size distribution (a, c) and grain structure analyses (b, d) of EBM and SLM Ti-6Al-4V samples

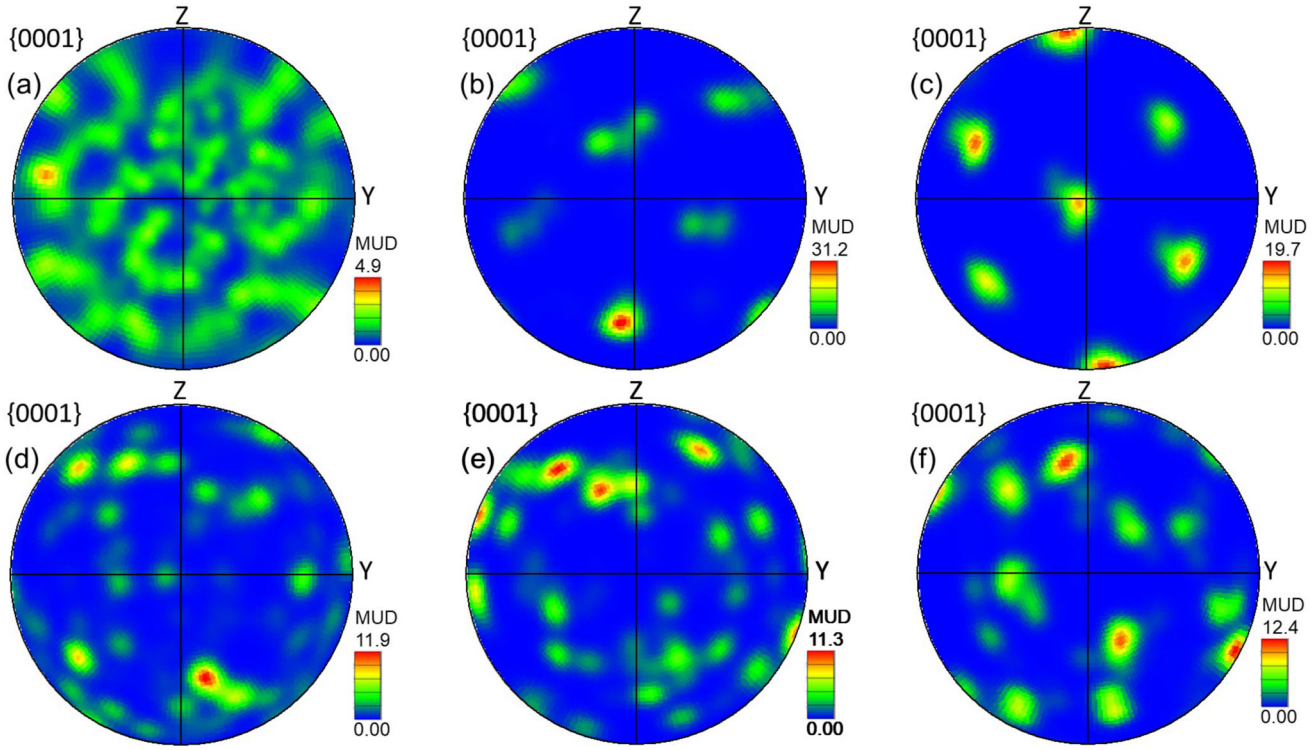

Fig. 9 Pole figures of (a) EBM-1, (b) EBM-2, (c) EBM-3, (d) SLM-1, (e) SLM-2, and (f) SLM-3 with representing MUD values

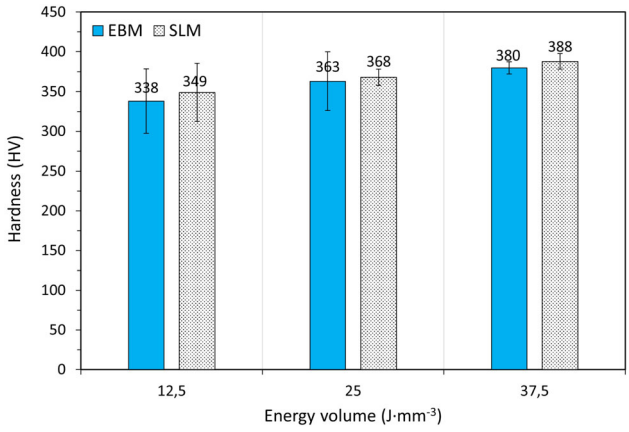

Fig. 10 The hardness results of Ti-6Al-4V alloys produced with different energy volumes through EBM and SLM processes

significant rise in relative density. When comparing EBM and SLM techniques at equivalent energy volume values, the hardness of EBM parts was consistently lower than that of SLM parts. This difference is mainly due to the presence of the martensite phase in the SLM microstructure, indicating faster cooling in the SLM technique.

The higher hardness in SLM parts compared to forged-Ti64 is well-known and is attributed to the presence of the martensite phase. As the energy volume increases in SLM parts, the size of the martensite structures also increases, although the hardness does not exhibit the Hall-Petch effect. Do (Ref 25) attributed this phenomenon to the high dislocation and heterogeneity in the martensitic structure.

Notably, the hardness of all alloys surpassed that of Ti-6Al-4V produced by traditional manufacturing methods. While Grade5 had a hardness of 349 HV, EBM-3 exhibited a hardness of 380 HV, and SLM-3 showed a hardness of 388HV. This discrepancy is attributed to the faster cooling rates inherent in AM techniques.

Tensile test results were conducted on similar samples, and the mechanical properties are given in Table 3.

The mechanical properties of the alloys were determined through tensile testing. With increasing energy volume in both the EBM and SLM groups, the yield stress (YS) and ultimate tensile strength (UTS) of the alloys increased. In other words, there is a positive correlation between energy density and mechanical properties and suggests that higher energy inputs lead to improved material strength. Since, higher energy inputs facilitate better fusion between powder particles, resulting in a denser microstructure (Fig. 2 and 3). Additionally, higher energy inputs promote grain refinement, leading to smaller grain sizes and a more uniform distribution of phases, and EBM alloys exhibited larger grain sizes compared to other SLM samples (Fig. 8). Due to these microstructural refinements, they impede dislocation movement and enhance grain boundary strengthening mechanisms, thereby contributing to improved material strength in SLM samples.

The lowest and highest UTS values were calculated as 448.7 and 1301.5 MPa, respectively, for samples EBM-1 and SLM-3. All SLM samples exhibited strength values > 930 MPa, surpassing those of wrought alloys (YS—850 MPa; UTS—930 MPa) cited in the ASM Handbook (Ref 11). However, among the EBM samples, only sample EBM-3 (1190.3 MPa) approached this standard. The better performance of SLM samples in terms of strength agrees with the previously reported studies (Ref 11, 13). This can be attributed

Table 3 Tensile test results of the of Ti-6Al-4V alloys produced with different energy volumes through EBM and SLM processes

Sample IDs	Energy volume, J mm^{-3}	Ultimate tensile strength, MPa	Yielding strength, MPa	E-modulus, GPa
EBM-1	12.5	448.7	434.1	12.0
EBM-2	25	838.8	805.3	20.9
EBM-3	37.5	1190.3	1132.4	24.8
SLM-1	12.5	1040.3	905.9	26.7
SLM-2	25	1125.9	1062.6	54.2
SLM-3	37.5	1301.4	1248.4	58.5

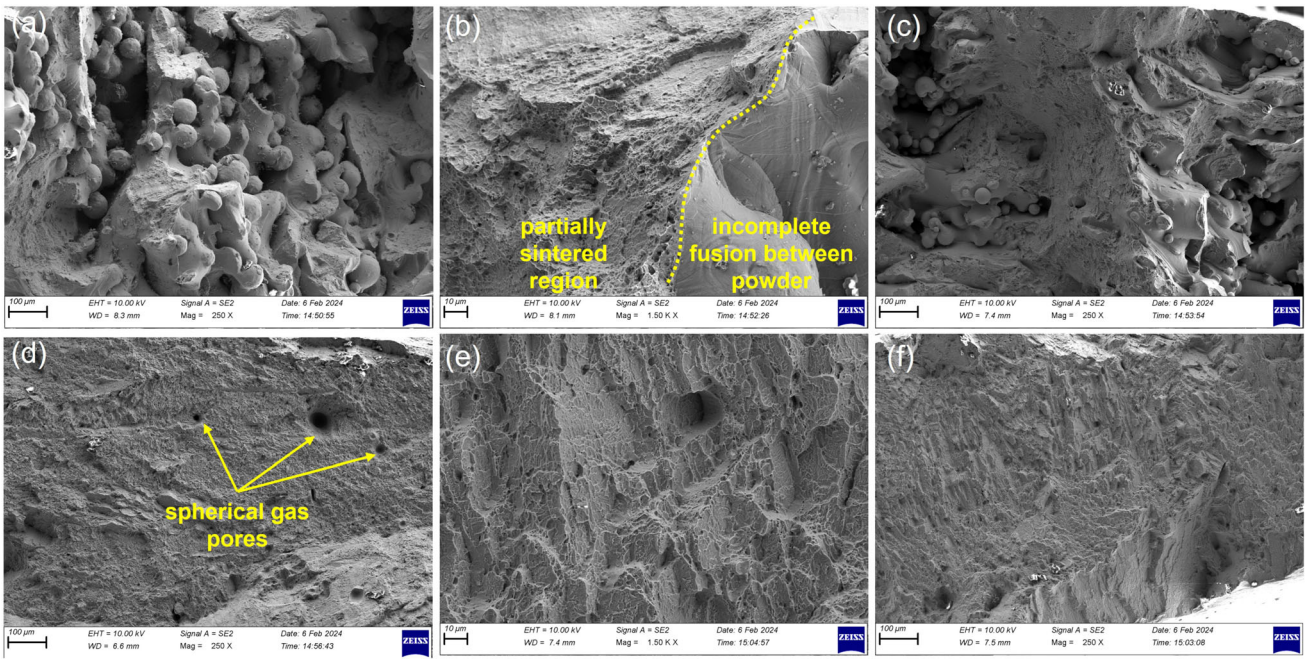

Fig. 11 Cross-section SEM images of (a) EBM-1, (b) EBM-1 (at higher magnification), (c) EBM-3, (d) SLM-1, (e) SLM-1 (at higher magnification), and (f) SLM-3 samples after tensile tests

to the formation of a martensitic microstructure and the presence of high dislocations in SLM-printed samples. Since, the absence of a martensitic structure in the EBM parts, due to slow cooling, may account for their comparatively lower strength. In can be said that the increased energy input influences phase transformations, favoring the formation of strengthen phases such as martensite in SLM-produced components.

Cross section SEM images of fractographies after the tensile test are shown in Fig. 11.

The fractured surface of the EBM-1 samples which exhibited the lowest UTS in the tensile tests revealed partially sintered particles with spherical shapes (Fig. 11a). These particles appeared to be loosely bonded and formed voids between the melted powders, indicating incomplete fusion between powder particles during the manufacturing process (Fig. 11b). The fracture initiation likely occurred at these regions, leading to a brittle fracture mechanism (Fig. 11b). Additionally, the observation of "necks" between powder particles suggests that some degree of bonding occurred, but the presence of spherical voids indicates inadequate bonding strength (Ref 33). This combination of factors could contribute to the reduced UTS observed in the EBM-1 sample. It was observed that as the energy volume increased, this effect diminished (Fig. 11c). However, for the SLM samples, the macrofracture surface is flat and the necking is not so obvious compared to EBM samples (Ref 34). In contrast to the EBM samples, the fracture surfaces of the SLM-1 sample (Fig. 11d) show a smoother appearance with higher sintered particles, indicating better fusion between powder particles. However, spherical gas pores are still evident (marked in Fig. 11d), which likely acted as stress concentrators and initiated fracture under tensile loading. At higher magnifications (Fig. 11e), the fracture surface of the SLM-1 sample reveals a more ductile fracture mode, with evidence of microvoid coalescence, indicating that despite the presence of gas pores, the material exhibited some plastic deformation before fracture. This ductile behavior is typical of the martensitic α' phase predominant in SLM Ti-6Al-4V alloys, which can absorb more energy before fracturing. For the SLM-3 sample (Fig. 11f), produced with the highest energy input, the fracture surface is relatively smoother and more homogeneous, with fewer visible defects compared to the SLM-1 sample. This suggests that the higher energy input improved the consolidation of the powder particles, reducing the prevalence of defects such as gas pores and leading to a more ductile fracture mode. The presence of fewer pores and a more continuous fracture surface likely contributed to the

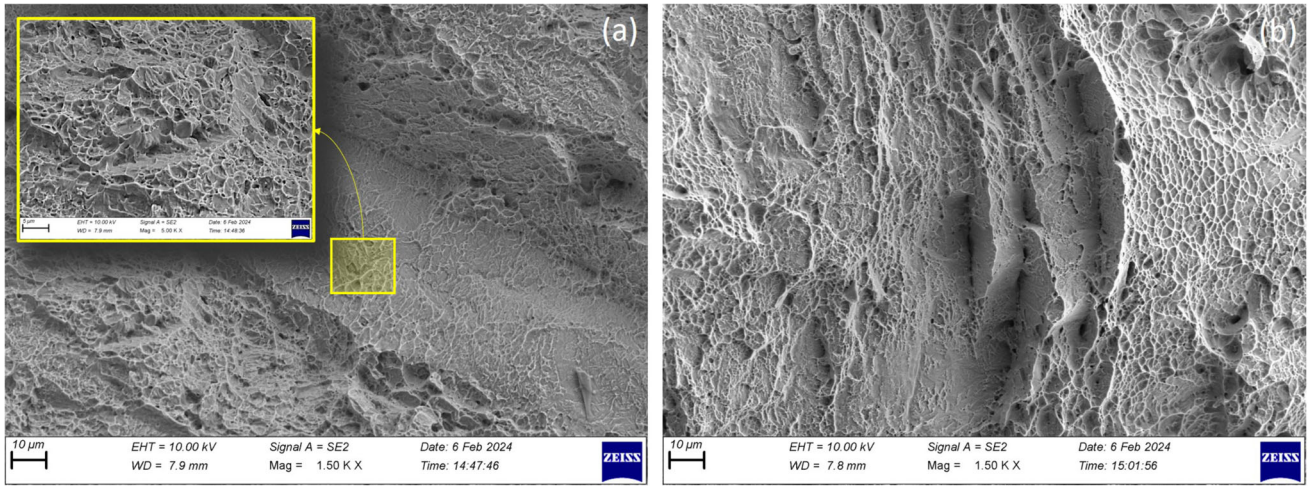

Fig. 12 Cross-section SEM images of (a) EBM-2 and (b) SLM-2 samples after tensile tests

higher UTS observed in the SLM-3 sample (Fig. 1f and Table 3).

In other words, with the increase in energy volume, the bonding between powder particles strengthened, leading to a reduction in porosity. Consequently, the presence of ductile fracture features on the fracture surface became more prominent (Fig. 12a). This phenomenon suggests that higher energy inputs promote better fusion between powder particles, resulting in denser microstructures with improved mechanical properties. Also, the phenomena are more prominent in SLM samples (Fig. 12b). A significant population of fine and deeper dimples at the tensile fracture surface indicates the extent of plastic deformation (Ref 11).

The PDS curves of the samples are presented in Fig. 13. Additionally, key corrosion parameters obtained from these curves are provided in Table 4.

Corrosion potential (E_{corr}) is a well-known indicator of the oxidizing power of the environment, while current density (I_{corr}) offers insight into the corrosion rate. In this context, the lowest and highest I_{corr} values among all samples were observed in SLM-1 and EBM-1 samples, respectively (Table 4). Similarly, for the EBM samples, an increase in energy density led to a decrease in corrosion rate, with EBM-1 exhibiting the highest corrosion rate of 197.36 $\times$ 10^{-3} mm year^{-1}, while EBM-2 and EBM-3 showed significantly lower rates of 1.02 $\times$ 10^{-3} and 4.97 $\times$ 10^{-3} mm year^{-1}, respectively. Conversely, the SLM samples displayed an increase in corrosion rate with increasing energy density, where SLM-1 had the lowest corrosion rate of 0.32 $\times$ 10^{-3} mm year^{-1}, and SLM-3 showed the highest rate of 64.45 $\times$ 10^{-3} mm year^{-1}. These findings suggest that the corrosion resistance of EBM samples improves with higher energy input, whereas SLM samples exhibit a deterioration in corrosion resistance under similar conditions. In other words, the corrosion rate of the SLM-1 sample is the lowest among all structures, indicating a higher polarization resistance. The highest corrosion resistance of the SLM-1 sample can be attributed to the martensitic structure of the SLM alloy. In fact, it has been reported that the presence of martensite phase in SLM Ti-6Al-4V alloy results in increased corrosion resistance (Ref 35, 36). On the other hand, faster cooling in SLM parts may have caused compression of the lattice structures, which may have led to lower corrosion resistance of other SLM samples in this study.

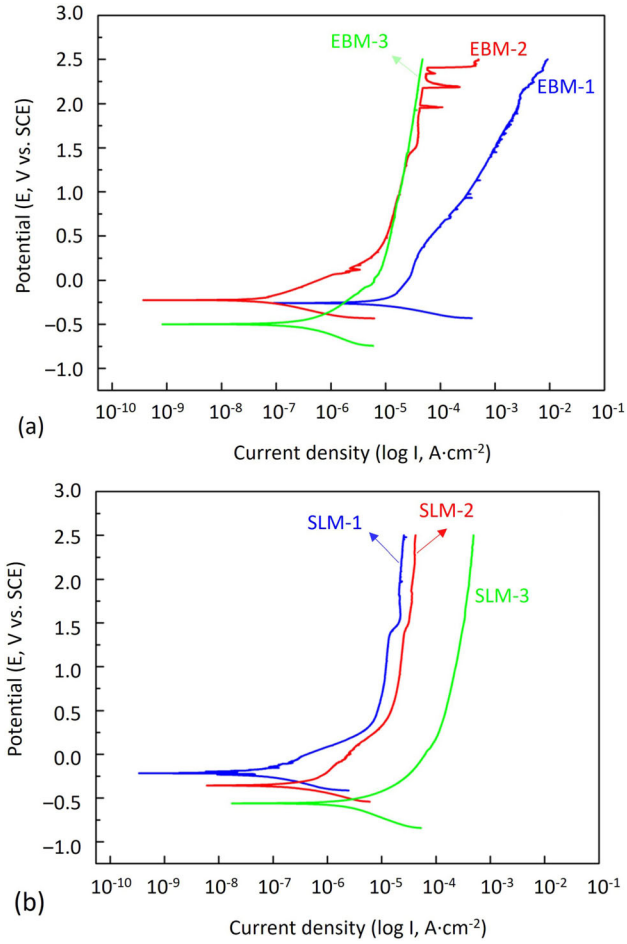

Fig. 13 Potentiodynamic polarization scanning (PDS) curves of the (a) EBM and (b) SLM samples

It should be also noted that despite both EBM-1 and SLM-1 samples having an energy density of 12.5 J mm^3, the porosity rate in the EBM-1 sample was considerably higher than in the SLM-1 sample. Porosities are known to hinder oxygen transfer in its inside, complicating the passivation of the structure. This explanation is also in good agreement with the surface

Table 4 Key corrosion parameters obtained from PDS curves of the samples

Sample ID	E_{corr}, V	I_{corr}, μA m^{-2}	Corr. rate $\times 10^{-3}$, mm year^{-1}
EBM-1	–0.258	17.000	197.36
EBM-2	–0.225	0.106	1.02
EBM-3	–0.498	0.554	4.97
SLM-1	–0.214	0.035	0.32
SLM-2	–0.356	0.633	5.67
SLM-3	–0.560	7.210	64.45

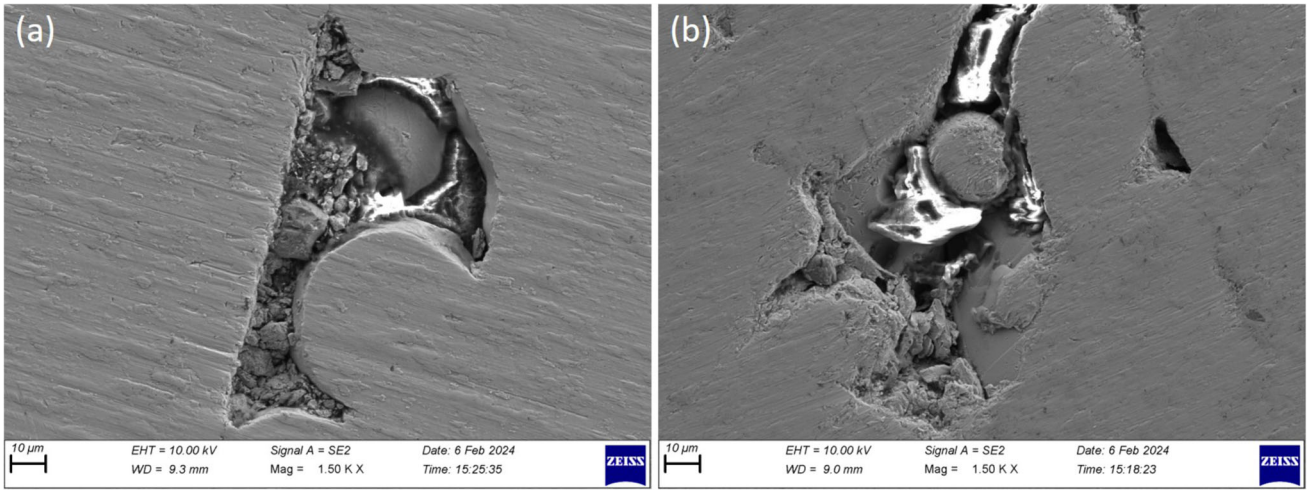

Fig. 14 SEM surface images of (a) EBM and (b) SLM samples after corrosion test

morphological observations conducted after corrosion (Fig. 13). The voids between partially melted powders served as initiation sites for corrosion in both EBM and SLM samples as shown in Fig. 14.

As shown in Fig. 11, a protective (nearly stable) passive surface layer was formed in all EBM and SLM samples, except for the EBM-1 sample. Notably, the EBM-1 sample exhibited a rapid increase in current density values in anodic regions of the polarization, indicating lower corrosion resistance compared to other samples. Although all PDS curves exhibit similar trends, it is evident that the polarization curves of EBM and SLM samples shifted to the right, except for EBM-1, with increasing energy volume. This shift signifies an increase in the corrosion susceptibility of the alloys with higher energy volume. The faster cooling in SLM parts, attributed to the absence of preheating, can lead to trapped cage structures, resulting in lower corrosion resistance. Furthermore, the martensite phase in the SLM microstructure, which retains the vanadium element, may reduce the corrosion resistance of the Ti-6Al-4V alloy. Previous studies on the corrosion resistance of Ti-6Al-4V alloys produced with EBM and SLM support these findings. For instance, Dai et al. (Ref 37) compared the corrosion resistance of SLM Ti-6Al-4V with the Grade 5 alloy produced by traditional manufacturing. The corrosion resistance of the oxide film on the surface of Grade 5 was found to be higher. Bai et al. (Ref 38) investigated the electrochemical behavior of EBM Ti-6Al-4V alloy and found that it exhibited better corrosion resistance than conventional wrought Ti-6Al-4V alloy. The I_{corr} value of the Ti-6Al-4V alloy produced with EBM was lower than the forged Ti-6Al-4V alloy.

By the way, when considering the phase structures, the difference in corrosion potential between the α and β phases can significantly influence the corrosion behavior (Ref 39). The α phase, with its hexagonal close-packed (HCP) structure, and the β phase, with its body-centered cubic (BCC) structure, exhibit distinct electrochemical properties (Ref 40, 41). In the EBM samples, these differences may have disrupted the stability of the protective oxide film on the surface, leading to higher corrosion currents. This phenomenon could explain why SLM samples, which predominantly feature a single-phase α' martensitic structure, tend to develop a more stable and uniform protective oxide film. In contrast, the presence of mixed α and β phases in EBM samples might have induced microgalvanic effects, further exacerbating corrosion (Ref 42).

Another contributing factor to this behavior may be the increase in laser/electron beam power which leads to an increase in martensite grain size (Ref 25). The laser power values selected in our study for SLM-1, SLM-2, and SLM-3 were 150, 300, and 360 mW, respectively. Similarly, Xiang et al. (Ref 43) demonstrated that the corrosion resistance of Ti-6Al-4V alloys produced with SLM decreased when a laser power of 360 mW was applied. A similar situation was observed in parts produced with EBM, except for EBM-1, which had a significantly higher I_{corr} value, indicating insufficient fusion in the structure.

Besides, the EBSD results revealed a distinctive microstructural variation between EBM and SLM Ti-6Al-4V samples,

which can be correlated with their corrosion behavior (Fig. 8). In EBM samples, particularly in EBM-1, an increase in grain size was observed which may have contributed to the increased corrosion susceptibility due to the presence of more grain boundaries and potential galvanic effect. Conversely, SLM samples exhibited a reduction in grain size with increasing laser energy densities. The finer grain structure in SLM samples positively influenced the corrosion resistance, likely due to the lower porosity and higher density. Fusion defects and irregular grain formations in EBM-1 may also be considered structural vulnerabilities that impact the corrosion resistance of the sample.

Considering all the results, future trends in AM of Ti-6Al-4V alloy could focus on optimizing energy density parameters to achieve desired material properties. Further research may explore the influence of additional process parameters, such as scan strategy, layer thickness, and powder characteristics, on the structural properties. Moreover, investigating post-processing techniques, such as heat treatment or surface finishing, could enhance the performance and reliability of the produced components. Additionally, studies on the long-term stability and durability of additively manufactured Ti-6Al-4V parts in various service environments would provide valuable insights for their practical applications. Overall, continued advancements in AM technologies and process optimization strategies will pave the way for broader utilization of Ti-6Al-4V alloy in diverse industrial sectors such as biomaterial, automotive, or aircraft.

4. Conclusions

In this study, the effect of the production parameters on the parts produced with SLM and EBM was investigated. The following conclusions can be drawn from the above study:

- Microstructural examinations have revealed that Ti-6Al-4V parts produced through SLM primarily consist of the α' (martensite) phase, while those produced through EBM are primarily composed of the α phase with a small amount of the β phase.
- Hardness and relative density increased in both the EBM and SLM samples with the increase in energy density. However, this increase was more pronounced in SLM samples compared to EBM samples due to the formation of the martensitic phase and rapid cooling.
- Except for the EBM sample built with an energy volume of 12.5 J mm^{-3}, a density of over 90% was achieved in all samples at all high-energy input.
- Similarly, in samples built with 25 and 37.5 J mm^{-3}, the hardness value was above 360 HV, significantly higher than the hardness value of Grade 5 Ti-6Al-4V alloy (349 HV).
- The lowest and highest ultimate tensile strength (UTS) values were calculated as 448 and 1301 MPa for the EBM sample built with 12.5 J mm^{-3} and the SLM sample built with 37.5 J mm^{-3}, respectively. However, all SLM samples exhibited strength values $>$ 930 MPa, surpassing those of wrought Ti-6Al-4V alloys.
- EBM sample produced with 37.5 J mm^{-3} energy volume exhibited an increased average grain size of 1.71 μm, correlating with a higher beam energy density. In contrast, SLM samples demonstrated reduced grain size with increasing laser energy, illustrating distinct microstructural characteristics.
- Corrosion susceptibility was generally increased with increased energy volume in both EBM and SLM samples. Especially, recrystallization trends and grain size variations influenced corrosion behavior.
- The SLM sample, produced with a 12.5 J mm^{-3} energy volume, displayed the lowest corrosion current density (I_{corr}, 0.0353 μA cm^{-2}), signifying superior corrosion resistance attributed to a denser structure and the absence of preheating-induced stresses. In contrast, the EBM sample produced at the same energy density exhibited the highest corrosion rate, associated with high porosity and low density.

Acknowledgment

This work was supported by the Japan Society for the Promotion of Science (JSPS) under grant number JP23H00235 and CREST-Nanomechanics from the Japan Science and Technology Agency (JST) under grant number JPMJCR2194. The author also thanks the Scientific and Technological Research Council of Turkey (TUBITAK) BIDEB 2209B program (grant no: 1139B412100784) for their support.

References

1. C. Körner, Additive Manufacturing of Metallic Components by Selective Electron Beam Melting—A Review, *Int. Mater. Rev.*, 2016, **61**(5), p 361–377. https://doi.org/10.1080/09506608.2016.1176289
2. L. Zhang, Y. Liu, S. Li, and Y. Hao, Additive Manufacturing of Titanium Alloys by Electron Beam Melting: A Review, *Adv. Eng. Mater.*, 2018, **20**(5), p 1700842. https://doi.org/10.1002/adem.201700842
3. Y. Zhao, K. Aoyagi, K. Yamanaka, and A. Chiba, Role of Operating and Environmental Conditions in Determining Molten Pool Dynamics during Electron Beam Melting and Selective Laser Melting, *Addit. Manuf.*, 2020, **36**, p 101559.
4. P.K. Gokuldoss, S. Kolla, and J. Eckert, Additive Manufacturing Processes: Selective Laser Melting, Electron Beam Melting and Binder Jetting—Selection Guidelines, *Materials (Basel)*, 2017, **10**(6), p 672. https://doi.org/10.3390/ma10060672
5. A.T. Khanjar and N.H. Jasim, A Brief Review of Electron Beam Melting (EBM) Manufacturing of Ti-6Al-4V Alloy for Biomedical Applications, *J. Manuf. Innov.*, 2023, **1**, p 83–102.
6. N. Uçak, A. Çiçek, and K. Aslantas, Machinability of 3D Printed Metallic Materials Fabricated by Selective Laser Melting and Electron Beam Melting: A Review, *J. Manuf. Process.*, 2022, **80**, p 414–457. https://doi.org/10.1016/j.jmapro.2022.06.023
7. B. Dikici, Z. Esen, O. Duygulu, and S.G. Koc, Corrosion of Metallic Biomaterials, *Advances in Metallic Biomaterials: Tissues, Materials and Biological Reactions*. M. Niinomi, T. Narushima, M. Nakai Ed., Springer, Berlin, Heidelberg, 2015, p 275–303. https://doi.org/10.1007/978-3-662-46836-4
8. K. Aslantas, B. Demir, A.S. Guldibi, M. Niinomi, and B. Dikici, A Comparative Study on the Machinability of β-Type Novel $Ti_{29}Nb_{13}Ta_{4.6}Zr$ (TNTZ) Biomedical Alloys under Micro-milling Operation, *J. Manuf. Process.*, 2023, **92**(5), p 135–146. https://doi.org/10.1016/j.jmapro.2023.02.043
9. S. Liu and Y.C. Shin, Additive Manufacturing of Ti6Al4V Alloy: A Review, *Mater. Des.*, 2019, **164**, p 107552. https://doi.org/10.1016/j.matdes.2018.107552
10. S. Leuders, M. Thöne, A. Riemer, T. Niendorf, T. Tröster, H.A. Richard, and H.J. Maier, On the Mechanical Behaviour of Titanium Alloy TiAl6V4 Manufactured by Selective Laser Melting: Fatigue Resistance and Crack Growth Performance, *Int. J. Fatigue*, 2013, **48**, p 300–307. https://doi.org/10.1016/j.ijfatigue.2012.11.011
11. X. Zhao, S. Li, M. Zhang, Y. Liu, T.B. Sercombe, S. Wang, Y. Hao, R. Yang, and L.E. Murr, Comparison of the Microstructures and

Mechanical Properties of Ti-6Al-4V Fabricated by Selective Laser Melting and Electron Beam Melting, *Mater. Des.*, 2016, **95**, p 21–31. https://doi.org/10.1016/j.matdes.2015.12.135
12. L.-C. Zhang and H. Attar, Selective Laser Melting of Titanium Alloys and Titanium Matrix Composites for Biomedical Applications: A Review, *Adv. Eng. Mater.*, 2016, **18**(4), p 463–475. https://doi.org/10.1002/adem.201500419
13. X.P. Ren, H.Q. Li, H. Guo, F.L. Shen, C.X. Qin, E.T. Zhao, and X.Y. Fang, A Comparative Study on Mechanical Properties of Ti-6Al-4V Alloy Processed by Additive Manufacturing vs. Traditional Processing, *Mater. Sci. Eng. A*, 2021, **817**(May), p 141384. https://doi.org/10.1016/j.msea.2021.141384
14. W. Toh, P. Wang, X. Tan, M. Nai, E. Liu, and S. Tor, Microstructure and Wear Properties of Electron Beam Melted Ti-6Al-4V Parts: A Comparison Study against As-Cast Form, *Metals (Basel)*, 2016, **6**(11), p 284. https://doi.org/10.3390/met6110284
15. W. Zhang, P. Qin, Z. Wang, C. Yang, L. Kollo, D. Grzesiak, and K. Prashanth, Superior Wear Resistance in EBM-Processed TC4 Alloy Compared with SLM and Forged Samples, *Materials (Basel)*, 2019, **12**(5), p 782. https://doi.org/10.3390/ma12050782
16. H. Gong, K. Rafi, H. Gu, G.D. Janaki Ram, T. Starr, and B. Stucker, Influence of Defects on Mechanical Properties of Ti-6Al-4V Components Produced by Selective Laser Melting and Electron Beam Melting, *Mater. Des.*, 2015, **86**, p 545–554. https://doi.org/10.1016/j.matdes.2015.07.147
17. H.K. Rafi, N.V. Karthik, H. Gong, T.L. Starr, and B.E. Stucker, Microstructures and Mechanical Properties of Ti6Al4V Parts Fabricated by Selective Laser Melting and Electron Beam Melting, *J. Mater. Eng. Perform.*, 2013, **22**(12), p 3872–3883. https://doi.org/10.1007/s11665-013-0658-0
18. Z. Yu, Z. Chen, D. Qu, S. Qu, H. Wang, F. Zhao, C. Zhang, A. Feng, and D. Chen, Microstructure and Electrochemical Behavior of a 3D-Printed Ti-6Al-4V Alloy, *Materials (Basel)*, 2022, **15**(13), p 4473. https://doi.org/10.3390/ma15134473
19. X. Zhou, D. Xu, S. Geng, Y. Fan, C. Yang, Q. Wang, and F. Wang, Microstructural Evolution and Corrosion Behavior of Ti-6Al-4V Alloy Fabricated by Laser Metal Deposition for Dental Applications, *J. Mater. Res. Technol.*, 2021, **14**, p 1459–1472. https://doi.org/10.1016/j.jmrt.2021.07.006
20. J. Fojt, M. Fousova, E. Jablonska, L. Joska, V. Hybasek, E. Pruchova, D. Vojtech, and T. Ruml, Corrosion Behaviour and Cell Interaction of Ti-6Al-4V Alloy Prepared by Two Techniques of 3D Printing, *Mater. Sci. Eng. C*, 2018, **93**, p 911–920.
21. M.K. Zadeh, M. Yeganeh, M.T. Shoushtari, H. Ramezanalizadeh, and F. Seidi, Microstructure, Corrosion Behavior, and Biocompatibility of Ti-6Al-4V Alloy Fabricated by LPBF and EBM Techniques, *Mater. Today Commun.*, 2022, **31**, p 103502.
22. L.E. Murr, S.M. Gaytan, F. Medina, H. Lopez, E. Martinez, B.I. Machado, D.H. Hernandez, L. Martinez, M.I. Lopez, R.B. Wicker, and J. Bracke, Next-Generation Biomedical Implants Using Additive Manufacturing of Complex, Cellular and Functional Mesh Arrays, *Philos. Trans. R. Soc. A Math. Phys. Eng. Sci.*, 1917, **2010**(368), p 1999–2032. https://doi.org/10.1098/rsta.2010.0010
23. H. Gong, K. Rafi, H. Gu, T. Starr, and B. Stucker, Analysis of Defect Generation in Ti-6Al-4V Parts Made Using Powder Bed Fusion Additive Manufacturing Processes, *Addit. Manuf.*, 2014, **1–4**, p 87–98. https://doi.org/10.1016/j.addma.2014.08.002
24. T. Montalbano, B.N. Briggs, J.L. Waterman, S. Nimer, C. Peitsch, J. Sopcisak, D. Trigg, and S. Storck, Uncovering the Coupled Impact of Defect Morphology and Microstructure on the Tensile Behavior of Ti-6Al-4V Fabricated via Laser Powder Bed Fusion, *J. Mater. Process. Technol.*, 2021, **294**(August 2020), p 117113. https://doi.org/10.1016/j.jmatprotec.2021.117113
25. D. Do Khoa, *Microstructure Characterizing and Mechanical Properties of Selective Laser Melted Ti-6Al-4V Alloys*, University of Glasgow, Glasgow, 2021
26. A. Safdar, *A Study on Electron Beam Melted Ti-6Al-4V*, Lund University, Lund, 2012
27. M.K. Kolamroudi, M. Asmael, M. Ilkan, and N. Kordani, Developments on Electron Beam Melting (EBM) of Ti-6Al-4V: A Review, *Trans. Indian Inst. Met.*, 2021, **74**(4), p 783–790. https://doi.org/10.1007/s12666-021-02230-9
28. L. Thijs, F. Verhaeghe, T. Craeghs, J. Van Humbeeck, and J.P. Kruth, A Study of the Microstructural Evolution during Selective Laser Melting of Ti-6Al-4V, *Acta Mater.*, 2010, **58**(9), p 303–3312. https://doi.org/10.1016/j.actamat.2010.02.004
29. W. Xu, S. Sun, J. Elambasseril, Q. Liu, M. Brandt, and M. Qian, Ti-6Al-4V Additively Manufactured by Selective Laser Melting with Superior Mechanical Properties, *JOM*, 2015, **67**(3), p 668–673.
30. J. Han, J. Yang, H. Yu, J. Yin, M. Gao, Z. Wang, and X. Zeng, Microstructure and Mechanical Property of Selective Laser Melted Ti6Al4V Dependence on Laser Energy Density, *Rapid Prototyp. J.*, 2017, **23**(2), p 217–226. https://doi.org/10.1108/RPJ-12-2015-0193
31. D. Bhattacharyya, G. Viswanathan, R. Denkenberger, D. Furrer, and H.L. Fraser, The Role of Crystallographic and Geometrical Relationships Between α and β Phases in an α/β Titanium Alloy, *Acta Mater.*, 2003, **51**(16), p 4679–4691. https://doi.org/10.1016/S1359-6454(03)00179-4
32. N. Stanford and P.S. Bate, Crystallographic Variant Selection in Ti-6Al-4V, *Acta Mater.*, 2004, **52**(17), p 5215–5224. https://doi.org/10.1016/j.actamat.2004.07.034
33. M.R. Mazlan, N.H. Jamadon, A. Rajabi, A.B. Sulong, I.F. Mohamed, F. Yusof, and N.A. Jamal, Necking Mechanism under Various Sintering Process Parameters–A Review, *J. Mater. Res. Technol.*, 2023, **23**, p 2189–2201. https://doi.org/10.1016/j.jmrt.2023.01.013
34. K.M. Bertsch, T. Voisin, J.B. Forien, E. Tiferet, Y.I. Ganor, M. Chonin, Y.M. Wang, and M.J. Matthews, Critical Differences Between Electron Beam Melted and Selective Laser Melted Ti-6Al-4V, *Mater. Des.*, 2022, **216**, p 110533. https://doi.org/10.1016/j.matdes.2022.110533
35. I. Cvijović-Alagić, Z. Cvijović, S. Mitrović, V. Panić, and M. Rakin, Wear and Corrosion Behaviour of Ti-13Nb-13Zr and Ti-6Al-4V Alloys in Simulated Physiological Solution, *Corros. Sci.*, 2011, **53**(2), p 796–808. https://doi.org/10.1016/j.corsci.2010.11.014
36. A. Hemmasian-Ettefagh, C. Zeng, S. Guo, and J. Raush, Corrosion Behavior of Additively Manufactured Ti-6Al-4V Parts and the Effect of Post Annealing, *Addit. Manuf.*, 2019, **28**(October 2018), p 252–258. https://doi.org/10.1016/j.addma.2019.05.011
37. N. Dai, L.C. Zhang, J. Zhang, Q. Chen, and M. Wu, Corrosion Behavior of Selective Laser Melted Ti-6Al-4V Alloy in NaCl Solution, *Corros. Sci.*, 2016, **102**, p 484–489.
38. Y. Bai, X. Gai, S. Li, L.C. Zhang, Y. Liu, Y. Hao, X. Zhang, R. Yang, and Y. Gao, Improved Corrosion Behaviour of Electron Beam Melted Ti-6Al-4V Alloy in Phosphate Buffered Saline, *Corros. Sci.*, 2017, **123**(November 2016), p 289–296. https://doi.org/10.1016/j.corsci.2017.05.003
39. H. Zhang, C. Man, L. Wang, C. Dong, L. Wang, D. Kong, and X. Wang, Different Corrosion Behaviors between α and β Phases of Ti6Al4V in Fluoride-Containing Solutions: Influence of Alloying Element Al, *Corros. Sci.*, 2020, **169**, p 108605. https://doi.org/10.1016/j.corsci.2020.108605
40. R.P. Kolli and A. Devaraj, A Review of Metastable Beta Titanium Alloys, *Metals (Basel)*, 2018, **8**(7), p 506. https://doi.org/10.3390/met8070506
41. A. Sotniczuk, J.L. Gilbert, Y. Liu, M. Matczuk, W. Chromiński, D. Kalita, M. Pisarek, and H. Garbacz, Corrosion Resistance of β-Phase Titanium Alloys under Simulated Inflammatory Conditions: Exploring the Relevance of Biocompatible Alloying Elements, *Corros. Sci.*, 2023, **220**, p 111271. https://doi.org/10.1016/j.corsci.2023.111271
42. J. Yang, Y. Song, K. Dong, and E.-H. Han, Research Progress on the Corrosion Behavior of Titanium Alloys, *Corros. Rev.*, 2023, **41**(1), p 5–20. https://doi.org/10.1515/corrrev-2022-0031
43. S. Xiang, Y. Yuan, C. Zhang, and J. Chen, Effects of Process Parameters on the Corrosion Resistance and Biocompatibility of Ti6Al4V Parts Fabricated by Selective Laser Melting, *ACS Omega*, 2022, **7**(7), p 5954–5961.